Ore Geology Reviews 136 (2021) 104224

Contents lists available at ScienceDirect

Ore Geology Reviews

journal homepage: www.elsevier.com/locate/oregeorev

Hydrothermal activity during the formation of REY-rich phosphorites in the early Cambrian Gezhongwu Formation, Zhijin, South China: A micro- and nano-scale mineralogical study

Jieqi Xing [a,b,c], Yuhang Jiang [a,b], Haiyang Xian [a,b], Zeyang Zhang [a,b,c], Yiping Yang [a,b,c], Wei Tan [a,b], Xiaoliang Liang [a,b,c], Hecai Niu [a,b], Hongping He [a,b,c], Jianxi Zhu [a,b,c,*]

[a] CAS Key Laboratory of Mineralogy and Metallogeny and Guangdong Provincial Key Laboratory of Mineral Physics and Materials, Guangzhou Institute of Geochemistry, Chinese Academy of Sciences (CAS), Guangzhou 510640, PR China
[b] CAS Center for Excellence in Deep Earth Science, Guangzhou 510640, China
[c] University of Chinese Academy of Sciences, Beijing 100049, PR China

ARTICLE INFO

Keywords:
Hydrothermal activity
Phosphorites
Early Cambrian Gezhongwu Formation
South China
Rare earth elements and yttrium (REY)
Micro- and nano-scale mineralogy

ABSTRACT

The rare earth elements and yttrium (REY) are enriched in marine sedimentary phosphorites, which are an important REY resource. The formation of marine REY-rich phosphorites is a product of sedimentary deposition, while some geochemical studies of phosphorites suggest that they also have the characteristics of hydrothermal deposition. Hydrothermal modification can have an important effect on the distribution of REY and REY minerals in phosphorites, although there is no direct mineralogical evidence for such hydrothermal activity. In this study, we used transmission electron microscopy and other microbeam techniques to investigate the hydrothermal activity during the formation of marine sedimentary phosphorites in the early Cambrian Gezhongwu Formation, Zhijin, South China. Geochemical and mineralogical evidence shows that late hydrothermal events occurred after formation of the marine sedimentary phosphorites. The observed micro-scale hydrothermal veins (e.g., barite), micro- and nano-scale hydrothermal minerals (e.g., anatase and fluorite), and hydrothermally transformed minerals (e.g., fluorapatite and zircon) provide direct mineralogical evidence of later hydrothermal activity. The hydrothermal fluid involved in the phosphorite deposition might have been a low-temperature reduced fluid, which was enriched in F, Ti. Moreover, the late hydrothermal activity changed the REY patterns of some minerals (e.g., fluorapatite and zircon) in the phosphorites, although the hydrothermal activity was not the main factor that controlled REY enrichment in the phosphorites. Our results not only provide direct evidence for hydrothermal transformation of marine sedimentary phosphorites, but also a possible explanation for the bell-shaped rare earth element patterns in apatite, suggesting that the apatite would not provide a reliable reconstruction of the paleo-ocean environmental conditions.

1. Introduction

The global demand for rare earth elements (REEs) and yttrium (i.e., REY), which are critical for emerging technologies such as in the electronics industry and renewable energy resources, is increasing rapidly (Service, 2010; Chen et al., 2011; Kato et al., 2011; Chakhmouradian and Wall, 2012). More than 85% of the world's REY supply comes from two types of deposit in China (Kynicky et al., 2012; Xu et al., 2017). The first is in alkaline igneous and carbonatitic rocks (e.g., the Bayan Obo deposit in China, which supplies 80% of the light rare earth elements worldwide; Orris and Grauch, 2002; Kynicky et al., 2012), and the other type is regolith-hosted ion adsorption deposits in southern China, which supply much of the heavy rare earth elements worldwide (Bao and Zhao, 2008; Xu et al., 2017).

It is necessary to identify other economic REY-rich deposits to meet the rapidly increasing REY demand (Long et al., 2010). Marine sedimentary phosphate deposits enriched in extractable REY could represent a new type of REY deposit in the future (Emsbo et al., 2015; Peiravi et al., 2021). Such deposits are rich in middle and heavy REEs.

The origin of such a REY-rich phosphorite deposit in the early

* Corresponding author at: CAS Key Laboratory of Mineralogy and Metallogeny and Guangdong Provincial Key Laboratory of Mineral Physics and Materials, Guangzhou Institute of Geochemistry, Chinese Academy of Sciences (CAS), Guangzhou 510640, PR China.
E-mail address: zhujx@gig.ac.cn (J. Zhu).

https://doi.org/10.1016/j.oregeorev.2021.104224
Received 31 January 2021; Received in revised form 8 May 2021; Accepted 10 May 2021
Available online 13 May 2021

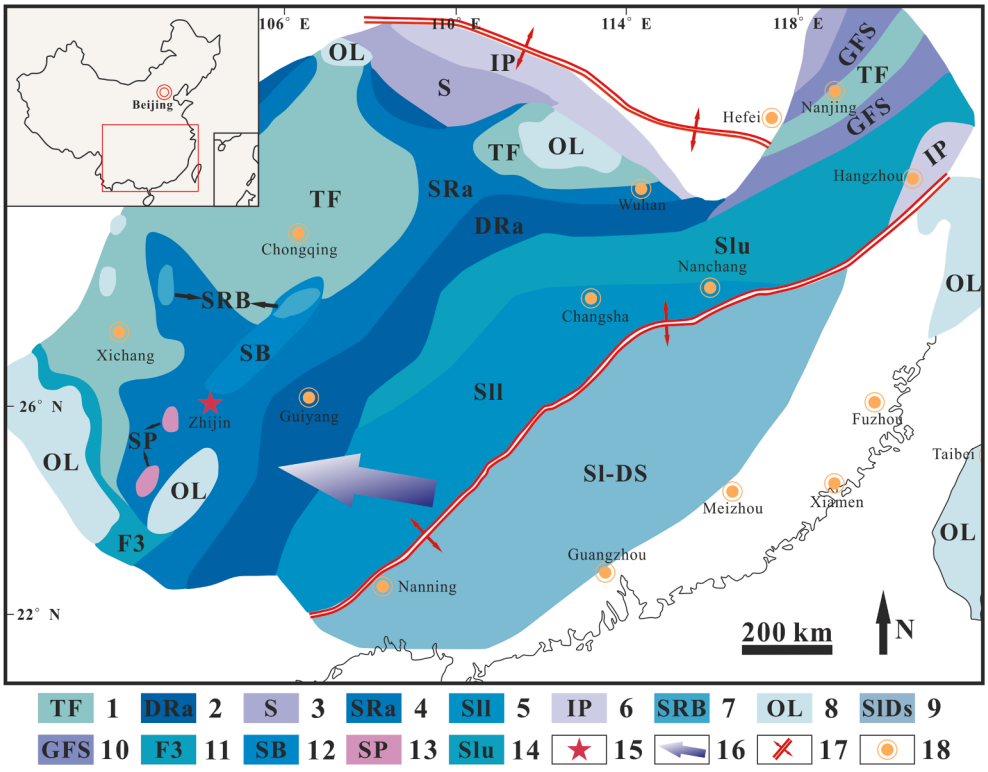

Fig. 1. Lithofacies and paleogeography of the early Cambrian in South China (after Chen et al., 2013). 1. Tidal flat; 2. deep-water ramp; 3. inner platform shoal; 4. shallow-water ramp; 5. lower slope; 6. isolated platform; 7. shallow-water ramp shoal; 8. old land; 9. continental slope–deep sea; 10. gentle slope; 11. foreshore; 12. storm shoal; 13. continental shelf; 14. upper slope; 15. REY-rich phosphorites in the Gezhongwu Formation; 16. transgressive direction; 17. constructive plate boundary; 18. cities.

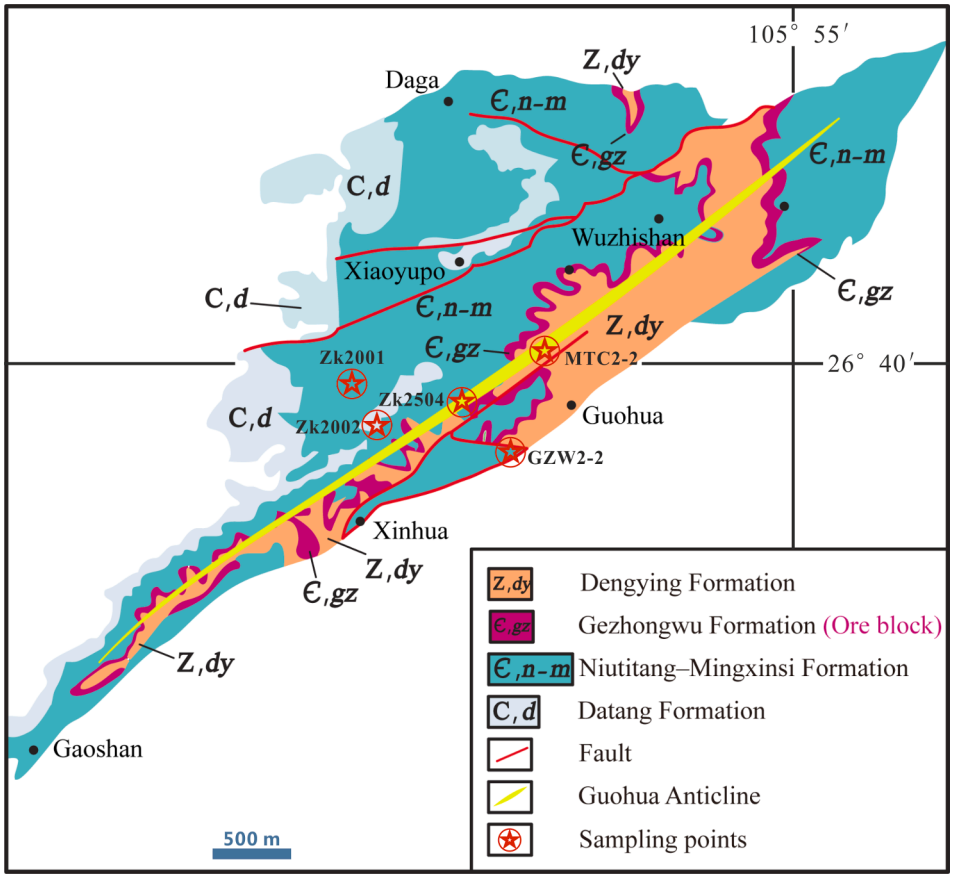

Fig. 2. Geological sketch map of phosphorite deposits in the early Cambrian Gezhongwu Formation in the Zhijin region (after Mao et al., 2015; Zhou et al., 2019).

Table 1
Geochemical and petrographical data for the Zhijin phosphate deposit (in *wt*%).

Sample	lithology description	SiO_2	Al_2O_3	Fe_2O_3	CaO	MgO	Na_2O	K_2O	TiO_2	MnO	P_2O_5	SO_3	BaO	LOI	Total
GZW-2-1	Phosphate cemented phosphorite	2.94	0.90	1.39	51.10	0.18	0.09	0.29	0.04	0.01	36.60	0.38	0.32	2.73	96.97
GZW-2-2	Phosphate cemented phosphorite	1.43	0.52	1.22	52.80	0.17	0.10	0.18	0.05	0.01	37.70	0.46	0.24	2.47	97.35
GZW-2-3	Phosphate cemented phosphorite	4.37	0.57	0.32	51.80	0.11	0.08	0.15	0.03	0.02	37.20	0.17	0.05	2.16	97.03
GZW-3-4	Phosphate cemented phosphorite	1.79	0.34	0.70	49.30	3.77	0.10	0.12	0.03	0.03	31.40	0.21	0.05	9.96	97.80
MTC-1-3	Dolomitic phosphorite	0.66	0.17	0.71	40.50	11.80	0.06	0.07	0.01	0.07	16.40	0.09	0.02	27.63	98.19
MTC-1-4	Phosphorous-bearing dolomite	1.02	0.10	0.65	34.20	17.65	0.03	0.04	<0.01	0.10	5.99	0.04	<0.01	39.83	99.65
MTC-2-2	Dolomitic phosphorite	3.96	0.83	0.73	42.40	8.21	0.06	0.30	0.02	0.05	21.40	0.13	0.03	19.98	98.10
MTC-2-3	Dolomitic phosphorite	2.23	0.59	0.68	37.20	13.40	0.04	0.21	0.01	0.09	12.40	0.11	0.08	31.45	98.49
ZK2001-79(Q)	Phosphorous-bearing dolomite	2.19	0.21	1.42	33.80	16.60	0.03	0.08	<0.01	0.17	6.51	0.05	0.01	38.13	99.20
ZK2001-79(S)	Phosphate cemented phosphorite	2.25	0.32	0.44	52.70	0.69	0.06	0.12	0.03	0.02	36.90	0.19	0.07	3.26	97.05
ZK2001-83.9	Dolomitic phosphorite	1.15	0.11	0.58	40.20	12.45	0.04	0.05	0.01	0.08	15.70	0.09	0.03	28.66	99.15
ZK2002-142	Phosphorous-bearing dolomite	10.86	0.86	3.06	28.00	15.55	0.02	0.28	0.02	0.44	3.20	0.02	<0.01	36.79	99.10
ZK2002-143.8	Phosphorous-bearing dolomite	10.76	0.97	1.49	32.10	12.80	0.03	0.34	0.04	0.20	9.43	0.61	0.02	29.89	98.68
ZK2002-144 (Q)	Phosphorous-bearing dolomite	9.05	1.42	1.65	32.40	13.10	0.04	0.49	0.05	0.20	9.51	0.51	0.01	30.24	98.67
ZK2002-144 (S)	Siliceous phosphorite	16.61	2.12	1.78	35.80	5.60	0.06	0.73	0.11	0.08	20.10	1.62	0.04	13.97	98.62
ZK2504-14.3	Siliceous phosphorite	20.47	8.02	4.52	32.20	1.09	0.06	2.48	0.22	0.51	23.30	0.11	0.07	4.55	97.60
ZK2504-15.1	Siliceous phosphorite	25.02	3.27	1.99	34.50	2.28	0.05	1.03	0.16	0.03	23.00	0.11	0.05	6.35	97.84
ZK2504-25.26	Dolomitic phosphorite	2.89	0.16	0.76	38.60	12.45	0.05	0.06	0.01	0.12	14.60	0.09	0.03	28.84	98.66
ZK2504-28.29 (Q)	Dolomitic phosphorite	2.28	0.60	0.62	48.30	4.09	0.10	0.20	0.03	0.04	29.70	0.19	0.06	11.37	97.58
ZK2504-28.29 (S)	Phosphate cemented phosphorite	1.39	0.44	0.68	52.90	0.91	0.13	0.13	0.04	0.02	36.40	0.24	0.06	4.50	97.84

Cambrian Gezhongwu Formation in China remains unclear. Previous studies (Emsbo et al., 2015; Fan et al., 2016; Chen et al., 2019) have shown that REY-rich phosphorites in the Gezhongwu Formation are of marine sedimentary origin. However, some studies have suggested that this deposit has characteristics typical of hydrothermal deposition, based on trace elements and fluid inclusions (Wang et al., 2004; Shi, 2005; Guo et al., 2017; Liu et al., 2019), although there is no direct evidence for hydrothermal activity. Submarine hydrothermal activity might be an important factor in REY enrichment, as such fluids are rich in REY (Michard et al., 1983; Han et al., 2017). Furthermore, hydrothermal activity can transform protogenetic minerals (Harlov, 2015; Li and Zhou, 2015; Liu et al., 2019) and effect REY distribution in phosphorites.

Mineral grains in some marine sedimentary phosphorites are relatively small (micro- or nano-scale) and difficult to study. Transmission electron microscopy (TEM) can reveal the structure and chemical composition of minerals at the nano-scale (Li and Zhou, 2015; Lee et al., 2016; Liao et al., 2019). In this study, we used a combination of TEM and other microbeam techniques to investigate phosphorites in the early Cambrian Gezhongwu Formation, Zhijin, South China. We identified several lines of mineralogical evidence for hydrothermal activity, such as barite veins, nano-anatase, micro- and nano-scale fluorite inclusions in dolomite, altered microcrystalline detrital zircon, and hydrothermally transformed fluorapatite. In order to determine the effects of the hydrothermal fluids on the incorporation of REY into the phosphorites, we compared the REY concentrations and patterns of hydrothermally transformed fluorapatite (Type II) with those of francolite without obvious hydrothermal modification (Type I). We also examined the effects of the hydrothermal fluids on microcrystalline zircon using TEM. Our results show that the late hydrothermal activity might have been caused by a low-temperature reduced fluid, which strongly modified the REY distribution in the phosphorites.

2. Geological setting

2.1. Sedimentary history

The early Cambrian was an important period of phosphorite formation. During this time, phosphorites in the Gezhongwu Formation were deposited in a transgressive setting following the regression in the late Sinian. These rocks were deposited at shallow-water ramp in the Yangtze platform (Pu et al., 1993; Chen et al., 2013; Fig. 1), and comprise dolomite, phosphate, and siliceous rocks. The largest phosphate deposit in China was formed in the early Cambrian, which was caused by the transgression and upwelling ocean currents. Previous studies have shown that the sedimentary facies include an old land–littoral tidal flat–shallow-water ramp (phosphate-bearing carbonate ramp), a deep-water ramp (phosphatic concretion-bearing siliceous ramp), and continental slope deep-water basin from southwest to east (Chen et al., 2013; Zhou et al., 2019; Fig. 1). When the Zhijin area began to undergo subsidence during the early Cambrian, the extensive transgression formed an open sea platform facies. The phosphorites of the Gezhongwu Formation in the Zhijin area were deposited in a shallow-water ramp setting (Pu et al., 1993; Chen et al., 2013; Fig. 1).

2.2. Deposit geology

The Zhijin phosphorite deposits in the early Cambrian Gezhongwu Formation are located in the southwestern “Central Guizhou Uplift”. The deposits are located in the Guohua anticline and are NE–SW-trending (Mao et al., 2015; Fig. 2). The Gezhongwu Formation is dominated by alternating dolomitic bioclastic phosphorite and phosphatic dolostone. The contact between the Gezhongwu Formation and the underlying Maolongjing section of the Dengying Formation is an unconformity. The upper section of Gezhongwu Formation are siliceous phosphorites, which are overlain by the lower section of the Niutitang Formation. (Wei

Table 2
Trace element data for the Zhijin phosphate deposit.

	Trace elements (in ppm)																	U/Th
	V	Cr	Co	Ni	Cu	Zn	Rb	Sr	Zr	Sb	Ba	Hf	Pb	Th	U	Ag	As	
GZW-2-1	13.0	28.0	68.6	71.8	34.4	91.0	6.20	923	20.0	116	2730	0.40	110	3.69	8.85	2.20	151	2.40
GZW-2-2	11.0	40.0	55.4	75.8	62.3	77.0	4.00	931	28.0	20.7	2100	0.50	129	3.71	12.9	5.36	58.5	3.46
GZW-2-3	7.00	16.0	3.30	5.70	70.8	77.0	3.20	868	21.0	15.3	388	0.40	1870	4.07	10.7	1.77	6.80	2.63
GZW-3-4	9.00	15.0	2.30	3.60	8.10	6.00	2.50	835	17.0	5.59	377	0.30	15.6	2.93	6.67	0.87	26.1	2.28
MTC-1-3	16.0	11.0	2.10	3.90	3.60	139	1.60	486	9.00	1.55	192	0.20	107	1.67	5.28	0.31	9.70	3.16
MTC-1-4	13.0	6.00	1.20	2.80	2.50	91.0	0.90	194	5.00	0.85	66.9	0.10	14.6	0.99	2.20	0.26	6.80	2.22
MTC-2-2	16.0	23.0	0.90	7.10	4.60	33.0	6.50	594	18.0	6.45	271	0.40	14.0	3.58	21.1	0.72	8.70	5.89
MTC-2-3	16.0	10.0	0.80	2.50	4.40	19.0	4.60	361	11.0	1.47	730	0.20	13.1	1.85	14.7	0.48	6.90	7.95
ZK2001-79(Q)	13.0	15.0	0.80	9.10	2.50	7.00	1.50	306	9.00	3.26	108	0.20	22.5	1.21	2.16	0.35	7.50	1.79
ZK2001-79(S)	14.0	19.0	1.11	7.40	5.00	3.00	2.60	1400	24.0	2.04	520	0.50	31.7	4.47	8.49	0.73	7.30	1.90
ZK2001-83.9	16.0	15.0	0.90	5.00	2.20	3.00	0.90	592	7.00	1.68	250	0.10	13.8	1.59	3.41	0.42	5.90	2.14
ZK2002-142	11.0	18.0	0.80	8.10	4.20	301	5.60	124	10.0	4.36	49.9	0.20	41.6	0.86	2.21	0.88	15.5	2.57
ZK2002-143.8	19.0	28.0	1.10	32.0	3.20	129	7.50	344	18.0	7.31	178	0.40	111	2.76	13.2	0.32	19.2	4.78
ZK2002-144(Q)	18.0	20.0	1.00	40.8	3.60	127	10.2	337	20.0	5.76	170	0.50	36.0	2.79	13.3	0.26	21.8	4.75
ZK2002-144(S)	26.0	31.0	1.60	36.0	8.10	67.0	16.2	683	43.0	9.03	336	1.00	55.6	5.66	23.6	0.47	40.3	4.17
ZK2504-14.3	36.0	33.0	5.50	2010	13.8	559	44.7	679	178	51.8	584	5.70	88.9	25.6	19.1	0.27	295	0.74
ZK2504-15.1	31.0	33.0	1.60	8.40	6.90	70.0	22.6	729	56.0	6.49	438	1.30	37.7	6.65	10.2	0.53	20.8	1.53
ZK2504-25.26	18.0	7.00	0.80	3.20	3.10	13.0	1.30	475	7.00	2.00	259	0.10	8.70	1.68	4.09	0.52	6.00	2.43
ZK2504-28.29(Q)	8.00	11.0	1.30	2.90	6.00	43.0	4.20	798	20.0	3.12	474	0.40	29.1	3.09	9.14	0.74	15.1	2.96
ZK2504-28.29(S)	6.00	20.0	1.20	4.60	5.20	59.0	2.90	962	26.0	6.06	455	0.60	28.4	3.70	12.5	0.96	17.5	3.36
Average	15.9	20.0	7.62	117	12.7	95.7	7.49	631	27.4	13.5	534	0.68	139	4.13	10.2	0.92	37.3	3.16
Upper crust (Taylor, 1985)	60.0	35	10.0	20.0	25.0	71.0	112	350	190	0.20	550	5.80	20.0	10.7	2.80	50.0	1.50	0.26
Enrichment factor	0.27	0.57	0.76	5.85	0.51	1.35	0.07	1.80	0.14	67.5	0.97	0.12	6.95	0.39	3.64	0.02	24.9	/

Table 3
Rare earth element and yttrium (REY) data for the Zhijin phosphate deposit.

	REY (in ppm)																Ce/Eu anomaly	
	La	Ce	Pr	Nd	Sm	Eu	Gd	Tb	Dy	Ho	Er	Tm	Yb	Lu	Y	Total	$Ce_{anom}N$	$Eu_{anom}N$
GZW-2-1	315	230	57.9	260	48.1	14.0	58.8	7.66	45.1	9.43	23.6	2.80	12.8	1.67	434	1521	0.39	1.24
GZW-2-2	330	237	58.8	256	44.8	13.2	57.0	7.42	45.7	9.61	25.1	2.89	13.7	1.86	499	1602	0.39	1.23
GZW-2-3	350	265	67.8	305	58.3	17.2	67.7	8.49	49.5	10.0	25.6	3.01	14.3	1.85	460	1704	0.40	1.29
GZW-3-4	261	164	43.4	186	31.4	8.29	40.4	5.45	34.6	7.37	19.7	2.33	11.7	1.50	382	1199	0.36	1.10
MTC-1-3	176	108	29.7	129	22.1	5.33	26.4	3.70	22.8	4.92	12.8	1.56	7.60	1.02	255	805	0.35	1.04
MTC-1-4	73.1	45.0	12.7	52.6	9.29	2.23	11.7	1.60	10.1	2.19	6.08	0.74	3.85	0.53	114	345	0.34	1.01
MTC-2-2	212	127	35.1	151	26.4	6.42	34.3	4.57	28.1	5.97	15.5	1.86	8.80	1.15	305	963	0.34	1.00
MTC-2-3	128	77.4	21.4	89.6	15.7	3.84	20.3	2.80	17.8	3.87	9.98	1.21	6.28	0.85	197	596	0.34	1.01
ZK2001-79(Q)	74.2	43.9	12.2	51.8	9.03	2.26	12.0	1.66	10.9	2.42	6.62	0.83	4.44	0.61	124	356	0.34	1.02
ZK2001-79(S)	368	213	59.9	258	44.5	10.7	57.3	7.77	48.1	10.3	26.5	3.11	14.8	1.94	522	1646	0.33	1.00
ZK2001-83.9	163	95.3	27.4	117	20.5	5.25	26.7	3.57	22.2	4.69	12.1	1.47	7.13	0.94	242	748	0.33	1.06
ZK2002-142	43.3	30.1	7.20	30.5	5.31	1.39	7.20	1.00	6.39	1.41	3.76	0.48	2.69	0.36	69.4	210	0.39	1.06
ZK2002-143.8	83.1	66.0	14.7	63.0	11.6	3.02	14.1	1.97	12.3	2.52	6.60	0.82	4.21	0.54	121	405	0.44	1.12
ZK2002-144(Q)	96.0	76.1	17.4	71.8	13.2	3.42	16.3	2.31	14.1	2.98	7.75	0.94	4.92	0.68	138	465	0.43	1.10
ZK2002-144(S)	186	151	35.3	154	27.7	6.64	34.0	4.68	28.3	5.79	14.9	1.82	8.98	1.16	266	927	0.43	1.02
ZK2504-14.3	312	285	68.2	295	54.1	11.8	65.6	9.21	56.5	11.4	29.9	3.63	18.2	2.41	493	1716	0.45	0.93
ZK2504-15.1	286	224	54.6	239	42.6	10.6	54.5	7.58	46.7	9.90	26.3	3.15	15.1	1.98	447	1469	0.41	1.04
ZK2504-25.26	142	86.6	25.8	108	19.3	4.83	24.6	3.36	20.5	4.41	11.3	1.39	6.69	0.84	228	687	0.33	1.04
ZK2504-28.29(Q)	256	146	43.8	177	32.7	7.20	38.9	5.59	35.0	7.43	20.1	2.41	11.8	1.52	355	1140	0.32	0.95
ZK2504-28.29(S)	324	184	56.8	228	41.6	9.52	50.1	7.32	43.8	9.38	24.5	3.06	14.0	1.86	426	1424	0.31	0.98
Average	209	143	37.5	161	28.9	7.35	35.9	4.89	29.9	6.30	16.4	1.98	9.59	1.26	304	996	0.37	1.06

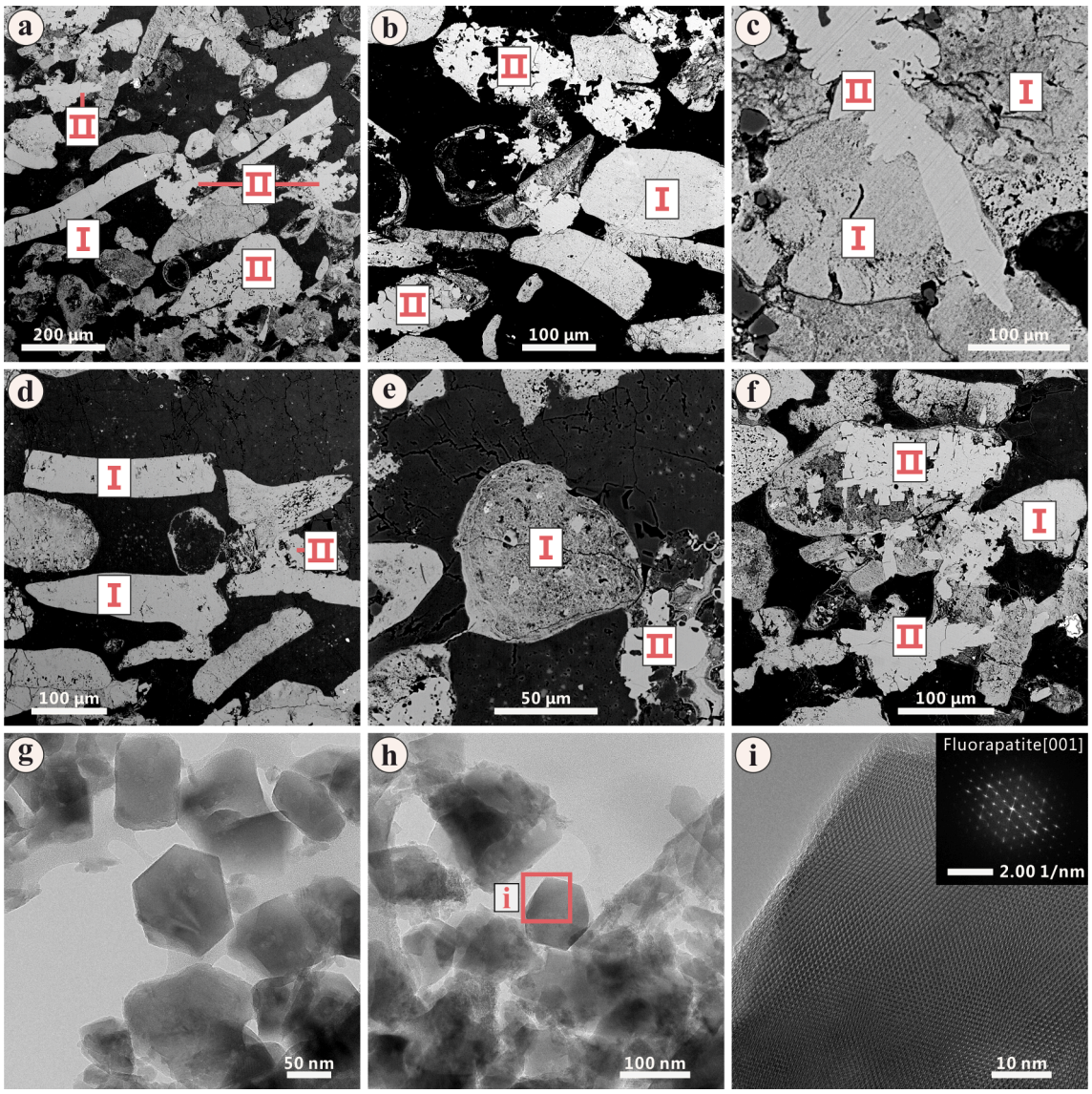

Fig. 3. SEM–BSE photomicrographs of the two types of fluorapatite and bright-field TEM images of nano-fluorapatites in the early Cambrian Gezhongwu Formation phosphorites. Type I = francolite; Type II = hydrothermal fluorapatite. (a–f) SEM–BSE photomicrographs; (g–h) bright-field TEM images of nano-fluorapatite in Type 1 francolite; (i) high-resolution TEM image of nano-fluorapatite from the red zone marked in (h), with a fast fourier transform (FFT) pattern.

et al., 2018; Chen et al., 2019; Zhou et al., 2019).

The Re–Os isotopic age of the black shale at the base of the Niutitang Formation in the Zhijin area is 522.9 ± 8.6 Ma, which constrains the latest age for the Gezhongwu Formation (Wei et al., 2018). In contrast, the best estimate of the age of the Gezhongwu Formation is 535.2 ± 1.7 Ma (Zhu et al., 2009). The Gezhongwu Formation in Guizhou and the Zhujiaqing Formation in Yunnan are correlative (Yang et al., 2005), so that deposition of the Gezhongwu Formation might have occurred between 535.2 ± 1.7 and 522.9 ± 8.6 Ma.

The phosphatic rocks are relatively low grade in P_2O_5 content, with an average content of 16–20 wt%, but contain abundant REEs and particularly high Y contents (approximately 35% of total REEs). The Y-group REEs comprise 45%–59% of the total REEs (Chen et al., 2013). The rare earth oxide (RE_2O_3) grade of the ore is 0.0541–0.1527 wt%, with an average of 0.1036 wt%. The Y_2O_3 grade is 0.0161–0.0583 wt%, with an average of 0.0371 wt% (Meng et al., 2015). In the Zhijin area, a total of 3.5 million tons RE_2O_3 resources of REY-rich phosphorites in the Gezhongwu Formation in early Cambrian have been identified (Guo et al., 2017).

3. Samples and analytical techniques

A total of 20 samples were collected and analyzed from the early Cambrian Gezhongwu Formation phosphorites (Fig. 2). The samples collected in five different areas were labeled GZW, MTC, ZK2001, ZK2002, and ZK2504. Based on major elements, the samples were divided into four types: phosphate–cemented phosphorites, dolomitic phosphorites, phosphorous–bearing dolomites, and siliceous phosphorites. All samples were made into 0.1 mm thick–sections for quantitative elemental analysis and mapping.

3.1. Whole-rock major elements

The rock powders were first heated to 900 °C for 90 min to remove organics and carbonates. Approximately 0.50 g of each pre-heated sample was then mixed with 4.00 g of $Li_2B_4O_7$, and the mixture was fused at 1200 °C and cooled to make a glass disc. Major elements were analyzed using a Rigaku ZSX100e X-ray fluorescence spectrometer. The analytical precision was <±1% (relative standard deviation; RSD).

Table 4
LA-ICP–MS rare earth element and yttrium (REY) data for the two types of francolite particles.

	REY (in ppm)																Ce/Eu anomaly	
	La	Ce	Pr	Nd	Sm	Eu	Gd	Tb	Dy	Ho	Er	Tm	Yb	Lu	Y	total	$Ce_{anom}N$	$Eu_{anom}N$
Type I																		
Type-I-1	376	222	67.0	291	52.6	12.8	66.6	8.48	50.3	10.6	24.4	2.65	13.7	1.36	527	1726	0.32	1.02
Type-I-2	409	207	57.2	247	44.1	9.43	56.4	6.95	43.7	9.79	24.5	2.89	15.4	1.74	539	1675	0.31	0.89
Type-I-3	344	165	47.0	203	36.0	8.37	44.1	6.18	38.1	8.87	22.9	2.69	14.1	1.63	491	1432	0.30	0.99
Type-I-4	325	156	43.6	190	33.3	7.30	42.8	5.48	35.0	7.68	19.9	2.34	12.0	1.54	448	1329	0.30	0.91
Type-I-5	228	122	36.5	171	31.7	7.39	38.6	5.25	32.0	7.34	16.7	1.93	9.29	1.06	373	1081	0.31	1.00
Type-I-6	373	195	53.4	240	43.7	9.50	52.0	7.28	42.2	8.95	22.5	2.74	13.3	1.58	495	1560	0.32	0.98
Type-I-7	316	153	41.5	177	32.0	6.93	39.9	5.52	33.4	7.35	18.4	2.26	11.4	1.43	416	1263	0.31	0.94
Type-I-8	373	198	54.6	247	45.4	10.1	54.0	7.09	44.8	9.69	24.0	2.72	13.3	1.67	516	1600	0.32	0.91
Type-I-9	363	184	53.8	242	44.3	10.1	53.5	7.35	43.3	9.91	23.7	2.75	13.1	1.74	512	1566	0.30	0.96
Type-I-10	373	189	52.8	240	41.6	9.17	52.6	7.01	43.1	9.26	23.4	2.61	13.9	1.61	504	1564	0.31	0.98
Type-I-11	347	171	47.2	213	37.0	8.48	45.6	6.18	38.2	8.10	21.1	2.52	12.5	1.53	459	1419	0.31	0.92
Detection Limit	0.002	0.002	0.002	0.016	0.010	0.004	0.010	0.002	0.004	0.001	0.003	0.001	0.002	0.002	0.001	\	\	\
Average	348	178	50.4	224	40.2	9.05	49.7	6.62	40.4	8.87	22.0	2.55	12.9	1.54	480	1474	0.31	0.95
Type 2																		
Type-II-1	184	141	45.5	222	40.5	10.2	49.2	6.58	39.1	8.01	18.6	1.91	7.75	0.88	377	1152	0.36	1.08
Type-II-2	114	89	31.9	170	36.6	12.9	46.8	6.42	36.4	7.27	15.8	1.54	6.36	0.62	334	909	0.34	1.47
Type-II-3	157	127	44.9	239	49.1	13.2	60.9	7.78	44.6	9.16	20.4	1.84	7.77	0.77	403	1187	0.35	1.13
Type-II-4	209	157	53.1	258	49.1	12.3	56.5	7.40	42.7	8.64	20.1	1.91	7.82	0.88	404	1288	0.34	1.10
Type-II-5	199	144	47.1	230	44.6	10.7	51.0	6.94	39.1	8.41	19.3	1.90	7.76	0.95	389	1201	0.34	1.05
Type-II-6	227	169	54.0	273	51.0	12.3	58.7	7.66	44.5	9.08	21.0	2.05	9.12	0.98	436	1375	0.35	1.06
Type-II-7	113	96	35.2	191	39.6	11.7	46.7	5.89	31.9	6.52	13.2	1.14	4.65	0.46	269	866	0.35	1.28
Type-II-8	129	105	37.6	189	38.1	11.0	47.3	6.03	33.4	6.75	14.8	1.29	5.48	0.52	298	924	0.35	1.21
Type-II-9	157	126	43.8	226	48.5	12.2	57.6	7.56	45.7	9.55	21.9	2.19	8.86	0.98	432	1200	0.35	1.22
Type-II-10	244	180	59.1	297	58.1	14.3	67.7	9.08	54.6	11.2	25.8	2.55	10.7	1.30	529	1564	0.35	1.09
Type-II-11	173	133	45.2	230	45.5	12.1	54.3	7.14	41.2	8.46	19.1	1.83	7.62	0.84	387	1167	0.35	1.07
Detection Limit	0.001	0.002	0.002	0.005	0.023	0.004	0.015	0.002	0.004	0.001	0.003	0.002	0.003	0.002	0.003	\	\	\
Average	173	133	45.2	230	45.5	12.1	54.3	7.13	41.2	8.46	19.1	1.83	7.63	0.83	387	1167	0.35	1.16

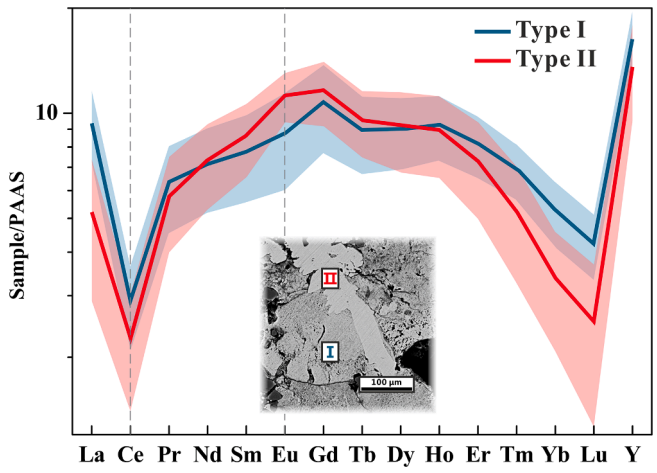

Fig. 4. Post-Archean Australian Shale (PAAS; Taylor, 1985)-normalized REY patterns for Type I and II fluorapatite, with SEM–BSE photomicrographs. Blue and red lines are the averages of Type I and II fluorapatite, respectively. The shaded area is the 95% confidence interval.

3.2. Whole-rock trace elements

Sample powders were heated to 550 °C for 3 h to eliminate organic material. Approximately 40.0 mg of each sample was then digested and analyzed using a Thermo Icap Qc inductively coupled plasma mass spectrometer (ICP–MS; Wang et al., 2018). Rhodium was added to each sample as an internal standard. The analytical precision was <±3% (relative standard deviation; RSD).

3.3. In situ major element analyses

For the *in situ* major element analyses, thin-sections were polished using diamond powder. The analyses were conducted with a JEOL JXA-8230 electron probe microanalyzer (EPMA) at the Key Laboratory of Mineralogy and Metallogeny (KLMM) in the Guangzhou Institute of Geochemistry (GIG), Chinese Academy of Sciences (CAS), Guangzhou, China. The analyses were carried out using a beam size of 4 μm, a 20nA beam current, and a 15 kV accelerating voltage. Peak and background counting times were 60, 30, 20, 10, 10, and 5 s for Si, S, Ca, P, F, and Cl, respectively. The Kα line was used for the analyses. Fluorine and chlorine were first analyzed during the analytical routine in order to minimize volatile loss. The data were reduced using the ZAF correction method. The standards used were as follows: francolite for Ca and P, BaF_2 for F, tugtupite for Cl, diopside for Si, and pyrite for S. The relative precisions were ±2% for Ca, P, and F, and ±5% for Si, Cl, and S (Xing and Wang, 2017).

3.4. In situ trace element analyses

Trace elements were analyzed by laser ablation (LA)–ICP–MS at the KLMM in the GIG, CAS. A Resonetics 193 nm ArF excimer LA system (GeoLasPro) was used for laser sampling, and the ion signal intensities were measured using an Agilent 7500a ICP–MS. The laser conditions were as follows: 29 μm laser spot size, 80 mJ laser energy, and 6 Hz laser frequency. Helium was used as a carrier gas. Each analysis consisted of a 20 s background measurement (laser off) followed by 45 s of data acquisition (laser on). The external standard was NIST SRM 610, and NIST SRM 612 was analyzed as quality control. The Ca content of francolite determined by EPMA was used as an internal standard. Data processing was undertaken using the ICPMSDataCal software (version 10.2; Liu et al., 2008).

3.5. Scanning electron microscopy

Thin-sections of rock samples were prepared for scanning electron microscopy (SEM) observations using a Phenom XL SEM equipped with a back-scattered electron (BSE) detector and an energy dispersive spectrometer (EDS), with a 15 kV accelerating voltage and 20nA beam current at the KLMM in the GIG, CAS.

3.6. Transmission electron microscopy

Thin-sections for TEM observations, with a thickness of approximately 100 nm, were prepared using a focused ion beam (FIB) and a FEI Scios dual beam system at the Institute of Geochemistry, CAS. The TEM observations were conducted using an FEI Talos F200S microscope operated at 200 kV at the KLMM in the GIG, CAS. Various techniques, including scanning TEM (STEM), high-resolution TEM (HRTEM), selected area electron diffraction (SAED), and energy dispersive spectroscopy (EDS), were used for morphological, structural, and compositional investigations.

4. Results

4.1. Major and trace element features of the phosphorite

Major and trace element data are listed in Tables 1 and 2, respectively. Based on geochemical features, the samples were divided into four lithological types, including phosphate-cemented phosphorite, dolomitic phosphorite, phosphorous-bearing dolomite, and siliceous phosphorite. The phosphate-cemented phosphorites contain 31.40–37.70 wt% P_2O_5, 49.30–52.90 wt% CaO, 0.11–3.77 wt% MgO, and 1.39–4.37 wt% SiO_2. The dolomitic phosphorites contain 12.40–29.70 wt% P_2O_5, 37.20–48.30 wt% CaO, 4.09–13.40 wt% MgO, and 0.66–3.96 wt% SiO_2. The phosphorous-bearing dolomites contain 3.20–9.51 wt% P_2O_5, 28.00–34.20 wt% CaO, 12.80–17.65 wt% MgO, and 1.02–10.86 wt% SiO_2. The siliceous phosphorites contain 20.10–23.30 wt% P_2O_5, 32.20–35.80 wt% CaO, 1.09–5.60 wt% MgO, and 16.61–25.02 wt% SiO_2. The Fe/Ti ratios vary from 10.67 to 153.00, with an average of 41.70. Compared with crustal abundances (Taylor, 1985), the phosphorites are relatively enriched in Ni, Sr, Pb, U, As, Mo, Sb, and Zn, and are relatively depleted in Cr, Th, Zr, Rb, and V (Table 2). The U/Th ratios range from 0.74 to 7.95 (average = 3.16), and only one sample has U/Th < 1.

4.2. REY geochemistry of the phosphates

The REY concentrations in 20 samples of the Zhijin phosphates range from 210 to 1716 ppm, with an average of 996 ppm (Table 3). The Ce anomaly (δCe) and Eu anomaly (δEu) were calculated as: $\delta Ce = Ce_N/\sqrt{La_N \times Pr_N}$; $\delta Eu = Eu_N/\sqrt{Sm_N \times Gd_N}$ (where the subscript N denotes normalization to Post-Archean Australian Shale [PAAS] values; e.g., $Ce_N = Ce_{sample}/Ce_{PAAS}$; Taylor, 1985). The δCe values are all < 0.5, with $\delta Ce_{average} = 0.37$. The δEu values of 15 samples are > 1, whereas those of the other samples are approximately 1 (average = 1.06).

4.3. Hydrothermally transformed fluorapatite

Both the phosphate-cemented and dolomitic phosphorites consist of fluorapatite grains. The REY elements are mainly concentrated in the fluorapatite of phosphorite (Jarvis et al., 1994; Fleet and Pan, 1995; Emsbo et al., 2015; Hughes and Rakovan, 2015). The SEM–BSE photomicrographs of fluorapatite grains show two types of morphologies with different contrast (Fig. 3a–f). Type I fluorapatite is autogenetic francolite, which is a mixture consisting mainly of nano-fluorapatite (50–200 nm; Fig. 3g–i), with biofossil shapes or detrital features that also appear "dirty" and relatively dark in the photomicrographs. Type II fluorapatite

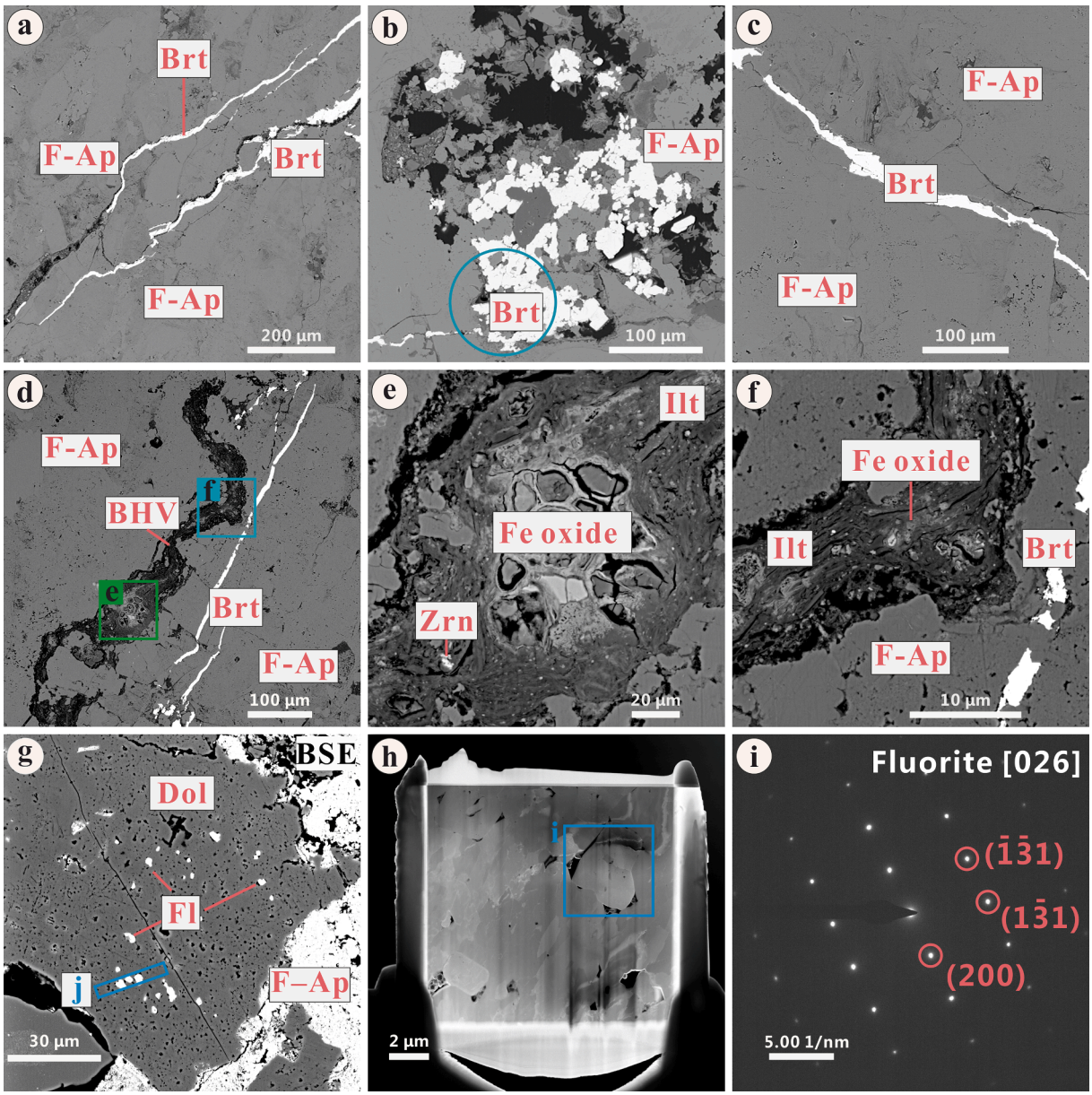

Fig. 5. SEM–BSE photomicrographs of hydrothermal veins in phosphorous-cemented phosphates. BHV = black hydrothermal vein; Brt = barite; F-Ap = fluorapatite; Zrn = zircon; Fe oxide = iron oxide; Ilt = Illite.

consists of hydrothermally transformed grains (10–50 μm), which appear "clean" and bright in SEM–BSE photomicrographs (Fig. 3a–f). From the relationship between Type I and Type II (Fig. 3c), it can be seen that Type II probably formed by fluid-aided dissolution-reprecitation from Type I. EMPA maps show that Type II fluorapatite contained higher contents of Ca, P and F (Fig. 6a–d). It is worth noting that Type II fluorapatite is mainly distributed around the black hydrothermal vein (BHV) (Fig. 6b). LA–ICP–MS analyses of the two types of fluorapatite (Table 4) show that the total REY concentrations of the two types are in the sequence of Type I > Type II. The PAAS-normalized REY patterns of the two types are shown in Fig. 4. The Ce and Eu anomaly diagram of the two types of fluorapatite (Fig. 14b) shows that from type I to type II, negative Ce anomaly change from 0.31 to 0.35 on average and Eu anomaly change from 0.95 (no positive anomaly) to 1.16 (positive anomaly) on average.

4.4. Ore petrography

Several fissure-filled barite and mixed minerals veins were observed in the phosphate samples by SEM–BSE imaging (Fig. 5). The chemical compositions of the veins were further constrained by EPMA elemental mapping (Fig. 6), which showed that Al, Ba, Si, and Fe are enriched in the BHVs, while Ba and S are enriched in the barite veins. The mineral phases in the veins were identified from Raman spectra and μ-XRD patterns. The results show that the barite veins consist mainly of a pure barite phase (Fig. 7). Given that the size of the mineral grains in the BHVs were too small to be identified by either Raman or μ-XRD methods, TEM techniques with FIB sampling were used to identify the mineral phases. The BHVs consist mainly of illite, goethite, nano-scale anatase, and microcrystalline zircon (Fig. 8). Hydrothermally transformed fluorapatite occurs near the BHVs (Fig. 6b).

In the BHVs, numerous microcrystalline detrital zircons (<10 μm) were observed by SEM (Fig. 9). The fine structure of the zircons was examined by FIB–TEM. The altered zircon (Fig. 10c) has the same crystal

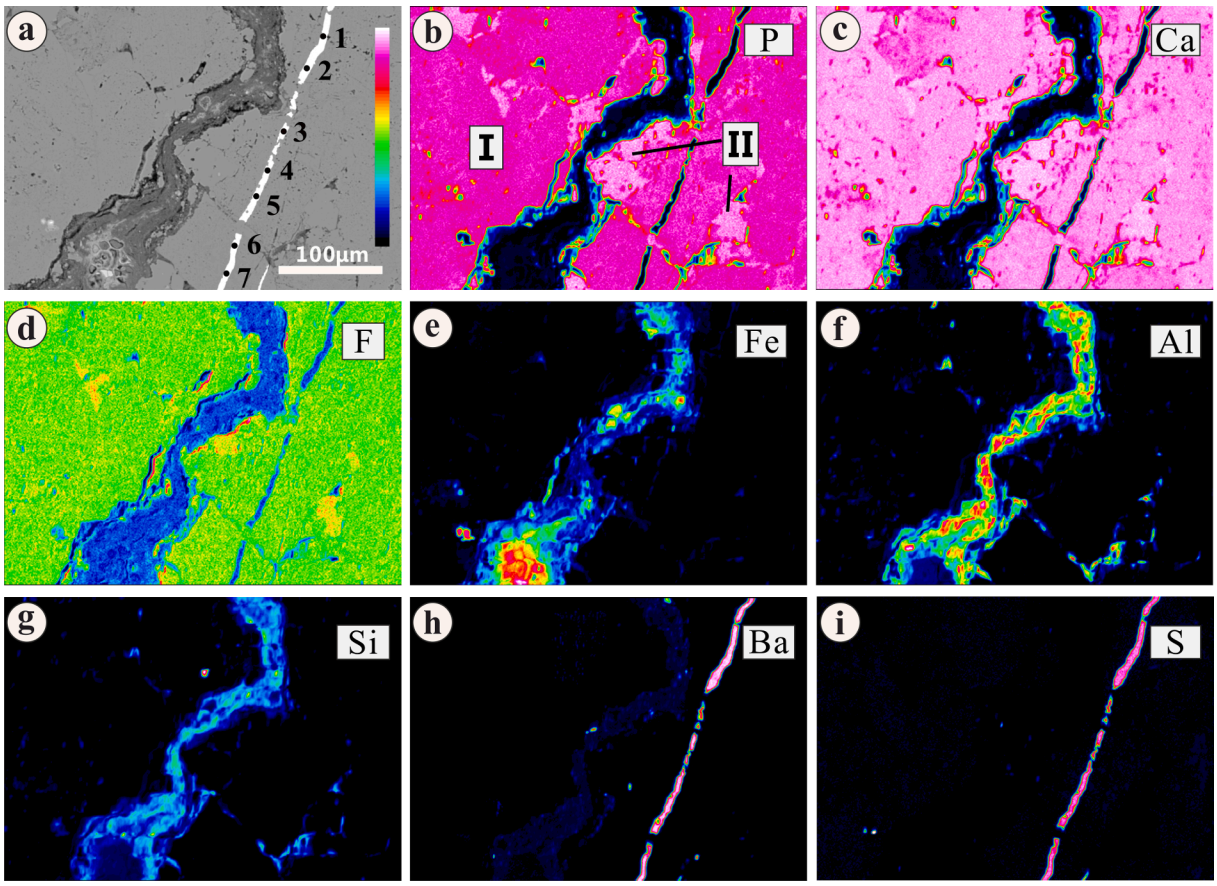

Fig. 6. EPMA elemental maps of phosphates in the barite and mixed-mineral veins. The numbered points (1–7) marked in (a) are sites where micro-Raman spectra were acquired. I and II in (b) denote autogenetic francolite and hydrothermally transformed fluorapatite, respectively.

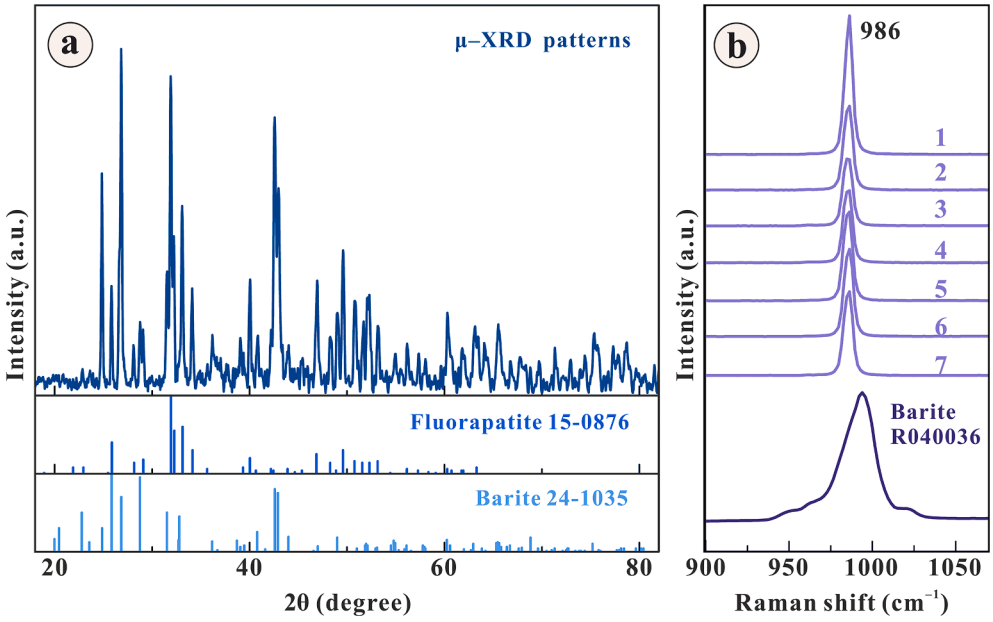

Fig. 7. (a) μ-XRD patterns of the blue zone marked in Fig. 5b and (b) Raman spectra for the barite veins. The spectra numbers correspond to those marked in Fig. 6a.

orientation as the unaltered zircon (Fig. 10d). The EDS maps showed that Y, Ti, Fe, and Al are higher in concentration in the altered zircons than in the unaltered zircon cores.

Numerous micro- and nano-scale fluorite inclusions are evenly distributed in dolomite in the dolomitic phosphorite (Fig. 11). The abundance of F-bearing micro-mineral inclusions were determined by SEM–EDS mapping (Fig. 11a–i). The mineral phases were further identified by TEM–SAED analyses (Fig. 11j–l). In addition, abundant pores were observed in the dolomites in SEM images.

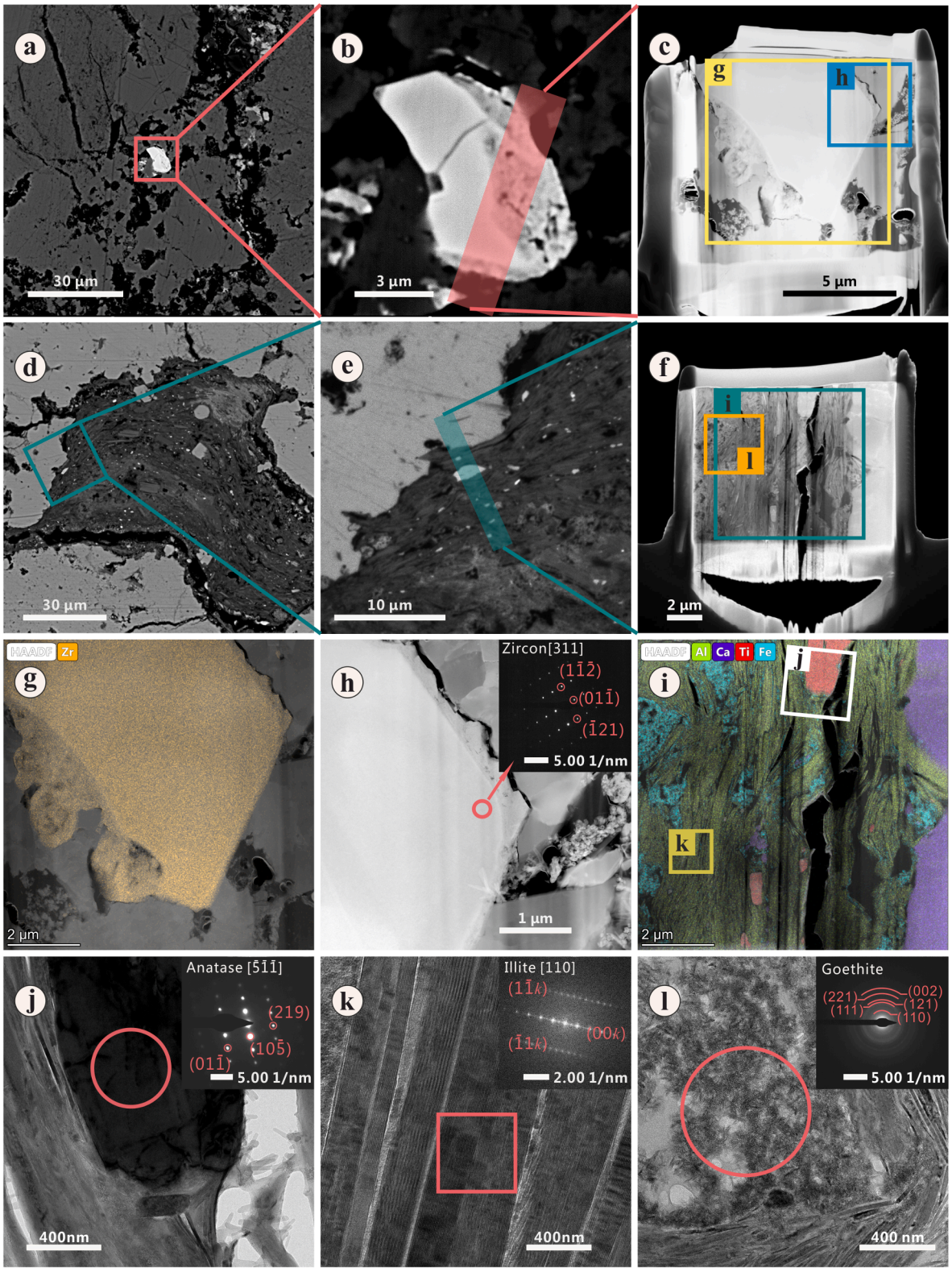

Fig. 8. Mineral compositions of the black hydrothermal veins. (a–b) SEM images of microcrystalline zircon; c: HAADF–STEM image of a thin-section sampled from the red zone marked in (b); (d–e) SEM images of nano-scale anatase and illite; (f) HAADF–STEM image of a thin-section sampled from the green zone marked in (e); (g) HAADF–STEM image and Zr map of the yellow zone marked in (c); (h) HAADF–STEM image of microcrystalline zircon with a selected area electron diffraction pattern; (i) HAADF–STEM image and Al, Ca, Ti, and Fe maps of the green zone marked in (f); (j) bright field TEM image of nano-scale anatase with a selected area electron diffraction pattern; (k): bright field TEM image of illite with FFT pattern; (l) bright field TEM image of goethite with a selected area electron diffraction pattern.

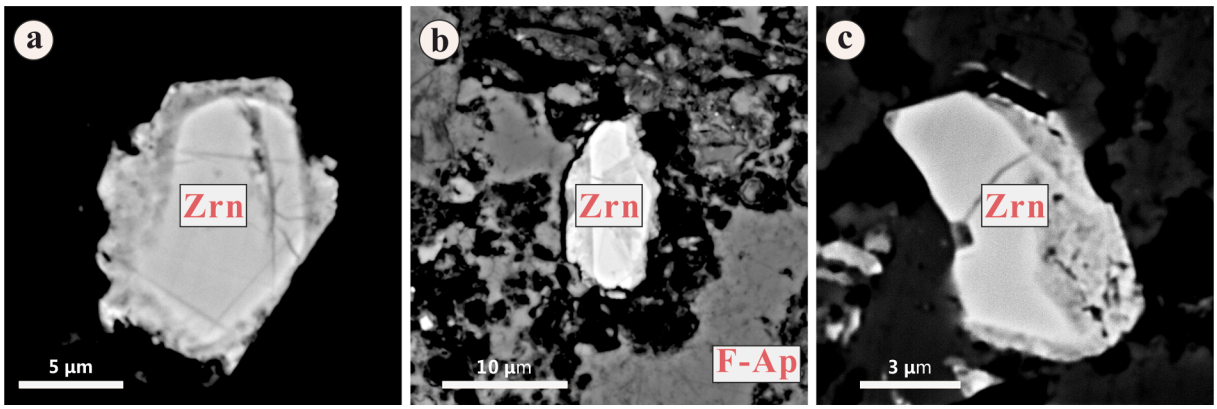

Fig. 9. SEM–BSE photomicrographs of microcrystalline detrital zircons in the black hydrothermal veins.

5. Discussion

5.1. Later hydrothermal alteration of the phosphorites

Based on major and trace element features of whole-rock, the Zhijin phosphorites probably experienced hydrothermal alteration. Immobile elements such as Fe, Mn, and Ti can be used to identify hydrothermal activity. Fe/Ti ratio can also be used to investigate the hydrothermal history of geological units (Boström, 1983). The average Fe/Ti ratios of the investigated samples is 41.70 (Table 1), which is higher than the threshold value of 20, indicating that the samples might be affected by hydrothermal activities. An Fe–Mn–(Cu + Ni + Co) × 10 ternary diagram can be used to identify the hydrothermal activity (Fig. 12). Most data plots in the hydrothermal deposition zone, which suggests the sedimentary phosphorites have experienced hydrothermal alteration.

Trace element data for the whole-rock samples can also be used to identify the origin. The U/Th ratio is commonly used for this, as the Th concentration is higher than that of U in most sedimentary rocks, as compared with other types of rocks. Therefore, U/Th > 1 indicates a hydrothermal deposition, whereas U/Th < 1 indicates a sedimentary origin (Rona, 1978). The U/Th ratios of the phosphorites are 0.74–7.95, with an average of 3.16, indicative of hydrothermal activity. Enrichments of certain trace elements can also be used as an indicator of hydrothermal deposition (Marchig et al., 1982; Boström, 1983). The enrichment factors (i.e., normalized to the trace element abundances of the upper crust) of As and Sb in the samples are 24.9 and 67.5, respectively, indicating that the phosphorites are hydrothermal in nature. Furthermore, the presence of hydrothermal micro- and nano-scale minerals (barite, anatase, and fluorite; Figs. 5 and 8) and hydrothermally altered fluorapatite and zircon (Figs. 3 and 8) provide direct evidence of later hydrothermal activity.

5.2. The nature of hydrothermal fluids

The chemical composition and redox state of hydrothermal fluids are key factors in controlling the process of hydrothermal alteration. Fluorapatite is the main constituent mineral in the studied phosphorites, and thus the relative elemental enrichment of hydrothermally transformed fluorapatite might reflect the chemistry of the hydrothermal fluids. PAAS-normalized REY patterns can reveal the sedimentary paleoenvironmental conditions (Grandjean et al., 1987; Ilyin, 1998; Jiedong et al., 1999), thus the REY patterns of the marine sedimentary francolite (Type I) (Fig. 4) can be used to disclose sedimentary paleoenvironmental conditions. The REY patterns of marine sedimentary francolites (Type I) exhibit marked negative Ce anomalies, no Eu anomalies, enrichment of middle REEs, and obvious enrichment in Y (Fig. 4). The negative Ce anomalies might indicate oxidized depositional conditions (Wright et al., 1987; Holser, 1997). In addition, Ce depletion and obvious enrichment in Y are the characteristics of seawater, which probably indicate that the REY of type I francolites from seawater. The hydrothermally transformed fluorapatite (Type II) has both negative Ce and positive Eu anomalies, indicating that the Eu anomalies were probably caused by the later hydrothermal transformation (Table 4; Fig. 4) (Michard et al., 1983; Mitra et al., 1994). The Ce and Eu anomaly diagram of the two types of fluorapatite (Table 4; Fig. 14b) shows that Ce anomalies and Eu anomalies are changed obviously from type I to type II. The change (from 0.31 to 0.35 on average; Table 4) of Ce anomaly indicates that the degree of oxidation was weakened, which may be caused by reduced fluid activity. The change (from 0.95-no positive to 1.16-positive) of Eu anomaly may also because of reduced fluid activity (Michard et al., 1983; Mitra et al., 1994). The positive Eu anomaly is characteristic of reduced hydrothermal fluids rather than oxidized (Yi et al., 1995). Since the formation environment of the type II fluorapatite was still an oxidizing environment, a large amount of Eu^{2+} in the hydrothermal fluid was oxidized to Eu^{3+}, which entered the type II fluorapatite lattice, so the PAAS-normalized REY patterns of type II fluorapatite are positive Eu anomalies. The REY patterns of whole-rock exhibit marked negative Ce anomalies, positive Eu anomalies, enrichment of middle REEs, and obvious enrichment in Y (Fig. 13). Therefore, the phosphorites probably formed in an oxidizing environment, and were then modified by a reduced fluid.

The nano-scale anatase observed in the BHVs (Figs. 5 and 8) indicates that the hydrothermal fluid was saturated with Ti. Titanium is prone to forming F-containing acid-based coordination complexes in F-bearing fluids, which can then cause large-scale migration of Ti (Collins et al., 1982; Rapp et al., 2010), even though it is one of the most immobile high-field-strength elements in nature. The enrichment of F in the hydrothermal fluid is further evident from the abundant micro- and nano-scale fluorite inclusions (Fig. 11). Therefore, the hydrothermal fluid was rich in both F and Ti. Altered microcrystalline detrital zircon is a good evidence of later hydrothermal fluid alteration. The STEM EDS mapping images show that the relative enrichment of high field strength elements, such as Y, U and Ti (Fig. 10h–l), in the altered edges of the zircon, which indicate that zircon was probably altered by F-rich hydrothermal fluid. The similar crystallographic orientation of the unaltered zircon cores and altered edges (Fig. 10c,d) indicates that the zircon was altered *in situ*.

The temperature of a hydrothermal fluid is another important parameter in understanding the origins of ore deposits. Firstly, anatase generally crystallizes at low temperatures and pressures (Doucet, 1967). Therefore, the large amount of nano-anatase in the BHVs might have formed from relatively low-temperature hydrothermal fluids. Secondly, hydrothermal barite, is generally formed in the low-temperature stage of mineralization (Yang et al., 2008; Zhang et al., 2020), which is an evidence of low-temperature hydrothermal activity in phosphorites. This temperature range is consistent with estimates from fluid inclusions

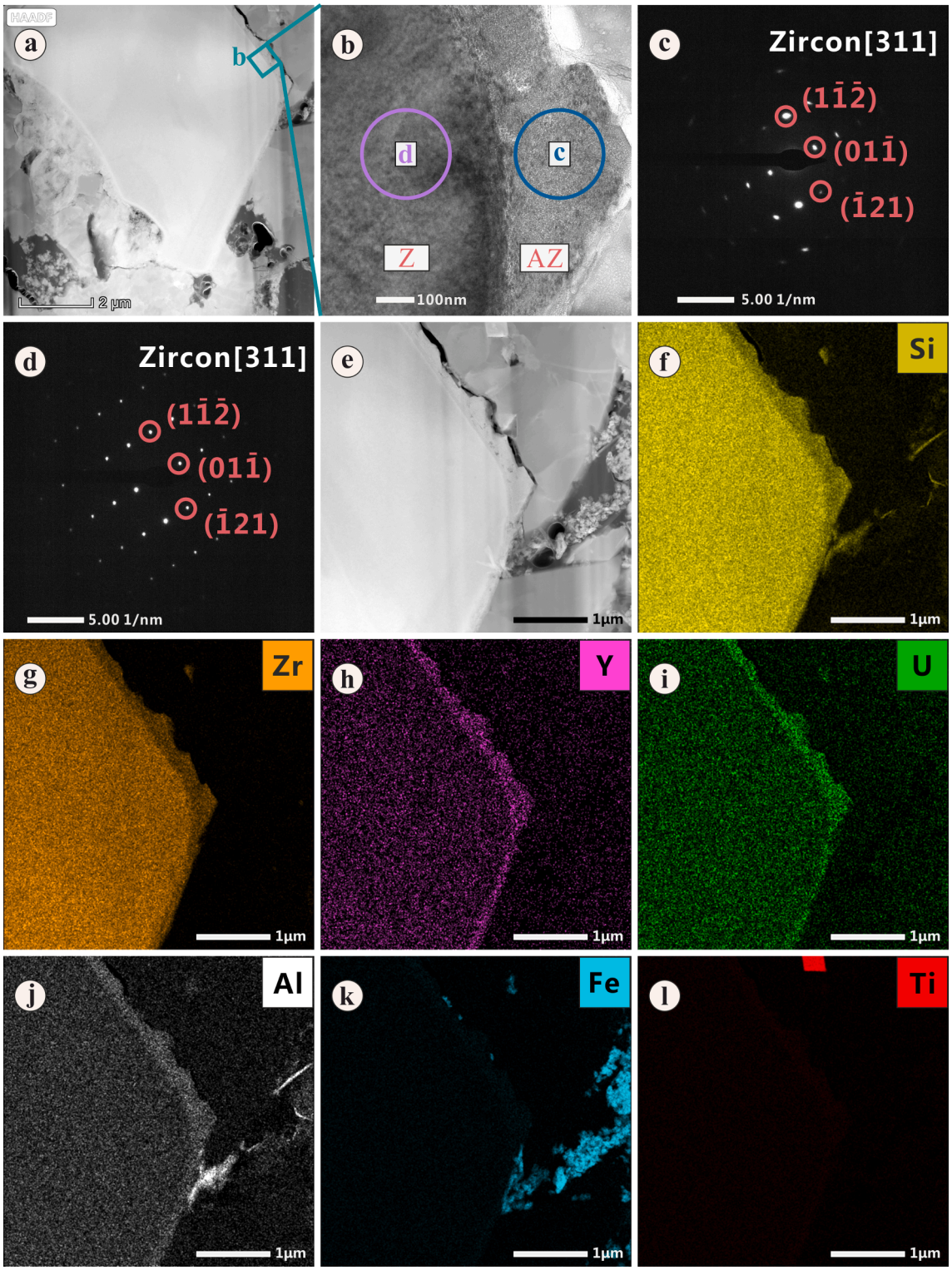

Fig. 10. HRTEM, SAED, and EDS element mapping images of altered zircon. Z = unaltered zircon; AZ = altered zircon. (a) HAADF–STEM image of altered zircon; (b) bright-field TEM images of the green zone marked in (a); (c) selected area electron diffraction image of altered zircon; (d) selected area electron diffraction image of an unaltered zircon core; (e) HAADF–STEM image of altered zircon; (f–l) Si, Zr, Y, U, Al, Fe, and Ti element maps of the same zone shown in (e), respectively.

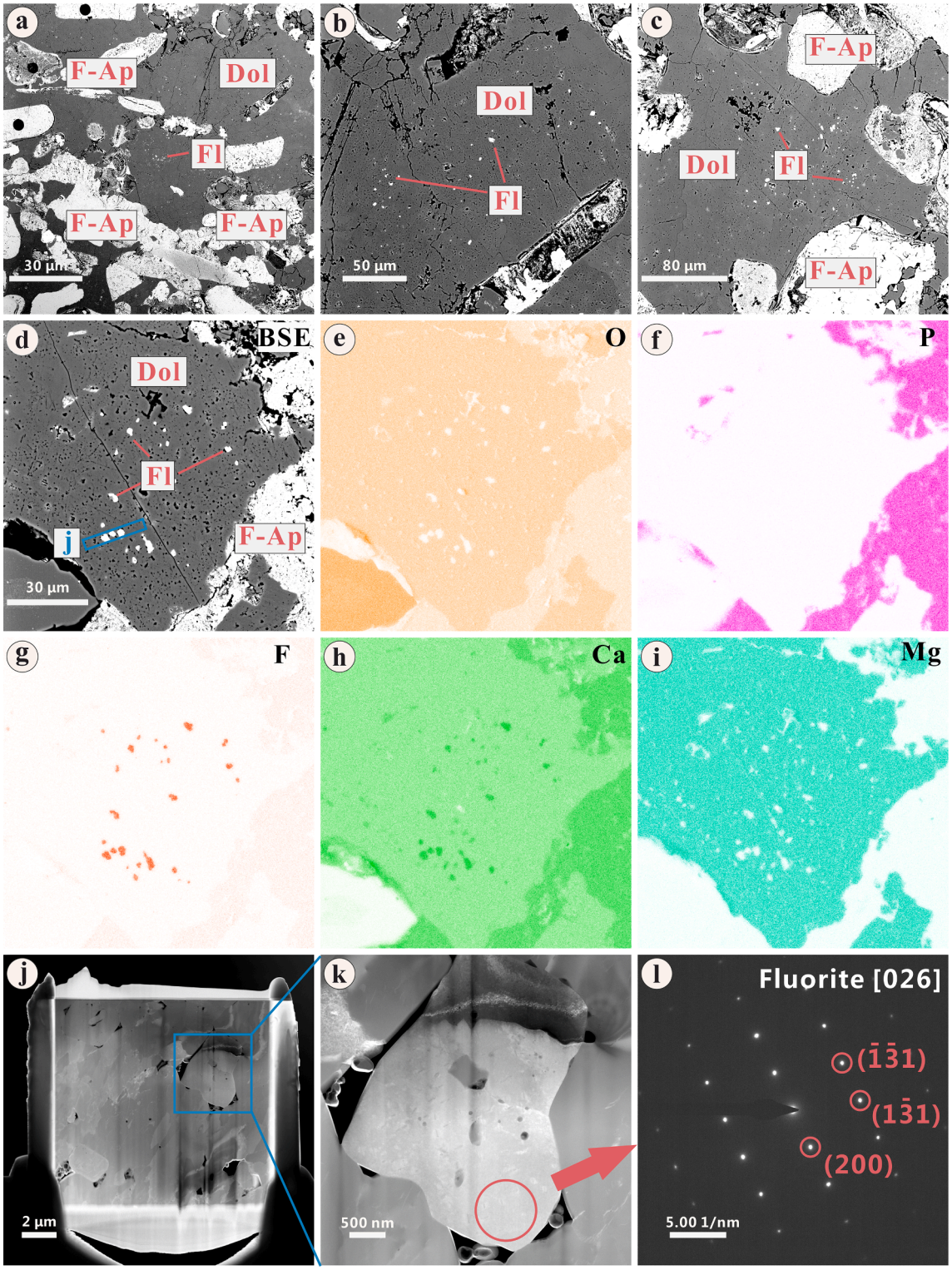

Fig. 11. SEM–EDS and TEM analyses of fluorite mineral inclusions in the phosphorites. F = fluorite; Do = dolomite; Fap = fluorapatite. (a–d) BSE images; (e–i) O, P, F, Ca, and Mg element maps of the same zone shown in (d), respectively; (j–k) HAADF–STEM images of a thin-section sampled from the blue box marked in (d); (l) selected area electron diffraction pattern of the position marked by a red circle in (k).

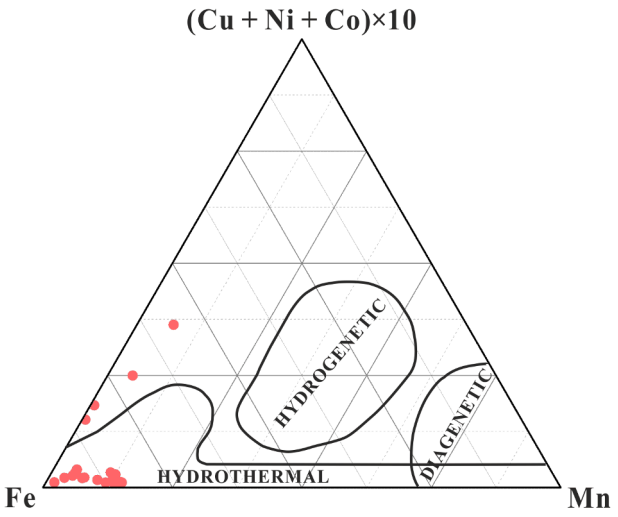

Fig. 12. Fe–Mn–(Cu + Ni + Co) × 10 ternary diagram for the studied phosphates (after Dekov et al., 2011).

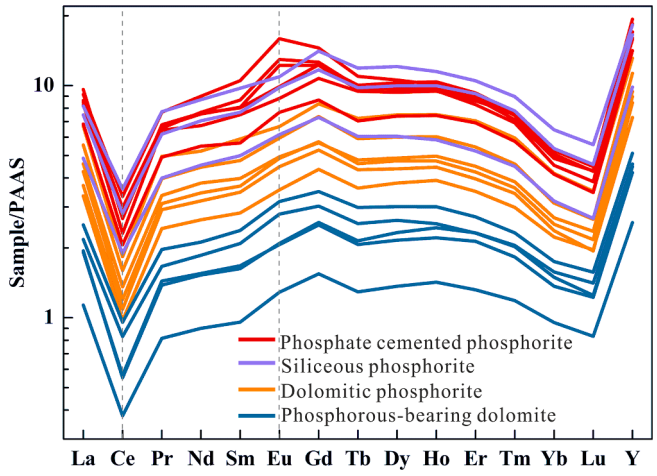

Fig. 13. Post-Archean Australian Shale (PAAS; Taylor, 1985)-normalized REY patterns of phosphorites in the early Cambrian Gezhongwu Formation in the Zhijin region.

(87.5–127.8 °C and 99.8–184.3 °C; Liu et al., 2019).

In summary, our mineralogical and *in situ* elemental analyses suggest that the hydrothermal fluid involved in the phosphorite deposition was a low-temperature reduced fluid, which was enriched in F, Ti.

5.3. *Influence of hydrothermal activity on the phosphorites*

Based on our results, the REY-rich phosphorites in the early Cambrian Gezhongwu Formation might have formed during normal marine sedimentation stage and later hydrothermal alteration stage. This produced the complex geochemical and mineralogical features in the phosphorites. The type I francolite is detrital formed during normal marine sedimentation stage, whereas the type II fluorapatite and other low-temperature hydrothermal minerals formed during hydrothermal activity stage.

The type I francolite might have had a biological origin or be an authigenic deposit. For biogenic francolite, adsorption of dissolved REY ions from seawater would be the dominant process that concentrates the REY elements, as the REY substitute in the Ca sites (Jarvis et al., 1994; Piper, 1999; Liao et al., 2019; Lumiste et al., 2019). The formation of authigenic francolite was an important sedimentary sink for reactive P in the oceans, and authigenic francolite is an important part of marine sedimentary phosphorite deposits (Ruttenberg and Berner, 1993; Schenau et al., 2000). The phosphate that formed the authigenic francolite originated by microbial degradation of organic matter, desorption from Fe oxides, and dissolution of marine faunal debris (Suess, 1981; Frohlich et al., 1983; Ruttenberg and Berner, 1993; Slomp et al., 1996). The REY are incorporated into the apatite lattice during the formation of francolite and/or absorption from seawater after its formation. The origin of the REY from seawater explains the similar initial REY contents and patterns of the biogenic and authigenic francolite.

Later hydrothermal activity was also important in controlling the formation of the REY-rich phosphorites, which changed the REY patterns of minerals such as fluorapatite and zircon. Hydrothermally transformed fluorapatite (Type II) formed from authigenic francolite (Type I) due to the effects of hydrothermal fluids. The REY substitute for Ca in the apatite lattice (Hughes et al., 1991; Fleet and Pan, 1997). The hydrothermal transformation resulted in the Type II fluorapatite being depleted in light and heavy REEs, and slightly enriched in the middle REEs (Table 4; Figs. 4 and 14). This may because the ionic radius of middle REE^{3+} are more suitable for the two Ca^{2+} sites in the apatite structure and have higher apatite/melt partition coefficients (Reynard et al., 1999; Hughes and Rakovan, 2015). Therefore, the transformation resulted in the loss of light and heavy REEs and formation of a positive Eu anomaly. As such, we speculate that F-rich hydrothermal

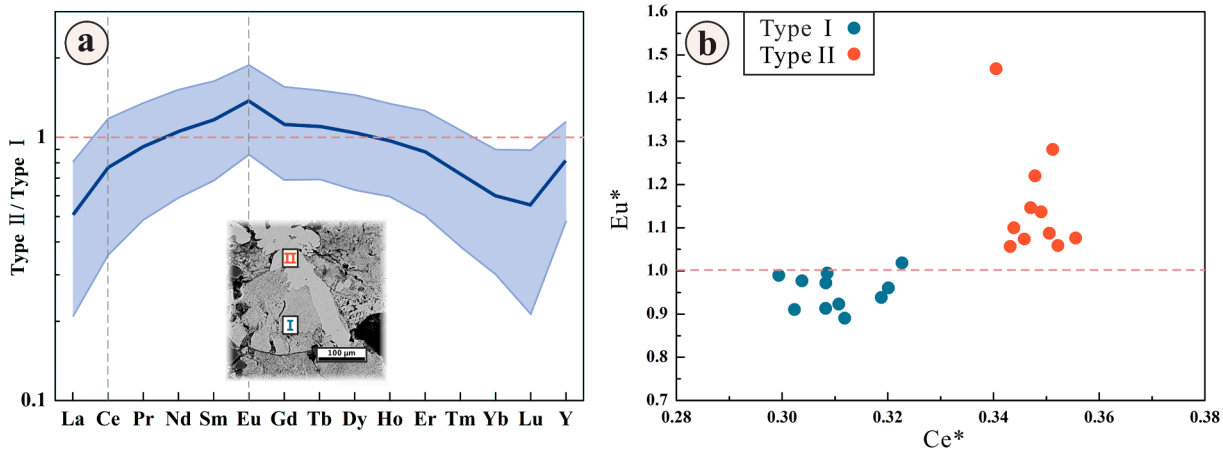

Fig. 14. (a) REY patterns and REY ratios of Type II fluorapatite divided by those of Type I francolite. The line is the average REY data, and the shaded area is the 95% confidence interval. (b) Ce and Eu anomaly diagram of the two types of fluorapatite.

transformation may be one reason for the bell-shaped REE patterns of apatite. Such apatite may not be a suitable proxy for paleo-ocean environmental reconstructions.

In summary, the later hydrothermal activity changed the REY patterns of various minerals in the phosphorites and the distribution of REY in the phosphorites. However, the hydrothermal activity was not the main reason for the REY enrichment in the phosphorites.

6. Conclusions

The REY-rich phosphorites in the early Cambrian Gezhongwu Formation formed by both normal marine sedimentation and hydrothermal deposition. The phosphorites formed in two stages. The first stage was the normal marine sedimentation stage, during which authigenic francolite (Type I) formed. The second stage was the low-temperature hydrothermal transformation stage, which hydrothermally transformed fluorapatite (Type II), altered zircon, and formed other hydrothermal minerals (e.g., barite, anatase, and fluorite).

In situ geochemical data and mineralogical evidence allowed the properties of the hydrothermal fluids involved in the Gezhongwu Formation phosphorite deposits to be determined. The hydrothermal fluids were low-temperature and reduced. In addition, the hydrothermal fluids might have been relatively rich in F, Ti.

The low-temperature reduced hydrothermal fluid changed the distribution of REY in the phosphorites and the REY patterns of minerals. The hydrothermally transformed fluorapatites are enriched in middle REEs, and depleted in light and heavy REEs. The hydrothermal fluid was not the main factor responsible for the REY enrichment. We speculate that F-rich hydrothermal activity could be one of the reasons for the bell-shaped REE patterns in apatite. Therefore, such REY signals of apatite should pay careful attention to paleo-ocean environmental reconstructions.

Declaration of Competing Interest

The authors declare that they have no known competing financial interests or personal relationships that could have appeared to influence the work reported in this paper.

Acknowledgements

This research was funded by the National Key R&D Program of China (Grant No. 2017YFC0602305), National Natural Science Foundation of China (Grant No. 41825003), Science Research Program of Guangzhou, China (Grant No. 201804020037), Guangdong Special Support Program (Grant No. 2019TX05L169), Science and Technology Planning Project of Guangdong Province, China (2020B1212060055).

References

Bao, Z., Zhao, Z., 2008. Geochemistry of mineralization with exchangeable REY in the weathering crusts of granitic rocks in South China. Ore Geol. Rev. 33 (3-4), 519–535.
Boström, K., 1983. In: Hydrothermal Processes at Seafloor Spreading Centers. Springer, pp. 473–489.
Chakhmouradian, A.R., Wall, F., 2012. Rare earth elements: minerals, mines, magnets (and more). Elements 8 (5), 333–340.
Chen, J., Yang, R., Wei, H., Gao, J., 2013. Rare earth element geochemistry of Cambrian phosphorites from the Yangtze Region. J. Rare Earth 31 (1), 101–112.
Chen, J., Yang, R., Zhang, J., 2019. Sedimentary and Element Geochemical Characteristics of Phosphorite-bearing Rocks at the Bottom of Cambrian in Yangtze area. Science Press, Beijing (in Chinese).
Chen, L.u., Liu, Y., Hu, Z., Gao, S., Zong, K., Chen, H., 2011. Accurate determinations of fifty-four major and trace elements in carbonate by LA-ICP-MS using normalization strategy of bulk components as 100%. Chem. Geol. 284 (3-4), 283–295.
Collins, W.J., Beams, S.D., White, A.J.R., Chappell, B.W., 1982. Nature and origin of a-type granites with particular reference to Southeastern Australia. Contrib. Mineral. Petrol. 80 (2), 189–200.
Dekov, V., Boycheva, T., Halenius, U., Billstrom, K., Kamenov, G.D., Shanks, W.C., Stummeyer, J., 2011. Mineralogical and geochemical evidence for hydrothermal activity at the west wall of 12 degrees 50 ' N core complex (Mid-Atlantic ridge): a new ultramafic-hosted seafloor hydrothermal deposit? Mar. Geol. 288 (1–4), 90–102.
Doucet, S., 1967. Synthese de la wolframite de la cassiterite et de lanatase a basse temperature. Bulletin De La Societe Francaise Mineralogie Et De Cristallographie 90 (1), 111.
Emsbo, P., McLaughlin, P.I., Breit, G.N., du Bray, E.A., Koenig, A.E., 2015. Rare earth elements in sedimentary phosphate deposits: solution to the global REE crisis? Gondwana Res. 27 (2), 776–785.
Fan, H., Wen, H., Zhu, X., 2016. Marine redox conditions in the early Cambrian ocean: insights from the lower Cambrian phosphorite deposits, South China. J. Earth Sci. 27 (2), 282–296.
Fleet, M.E., Pan, Y., 1995. Site preference of rare-earth elements in fluorapatite. Am. Mineral. 80 (3-4), 329–335.
Fleet, M.E., Pan, Y., 1997. Site preference of rare earth elements in fluorapatite: binary (LREE+HREE)-substituted crystals. Am. Mineral. 82 (9-10), 870–877.
Frohlich, P.N., Kim, K.H., Jahnke, R., Burnett, W.C., Soutar, A., Deakin, M., 1983. Pore water fluoride in Peru continental-margin sediments - uptake from seawater. Geochim. Cosmochim. Ac 47 (9), 1605–1612.
Grandjean, P., Cappetta, H., Michard, A., Albarede, F., 1987. The assessment of REE patterns and nD-143-ND-144 ratios in fish remains. Earth. Planet. Sc. Lett 84 (2–3), 181–196.
Guo, H.Y., Xia, Y., He, S., Xie, Z.J., Wei, D.T., Lei, B., 2017. Geochemical characteristics of Zhijin phosphorite type rare-earth deposit, Guizhou province, China. Acta Mineral. Sinica 37 (06), 755–763 (in Chinese with English abstract).
Han, T., Fan, H., Zhu, X., Wen, H., Zhao, C., Xiao, F., 2017. Submarine hydrothermal contribution for the extreme element accumulation during the early Cambrian, South China. Ore Geol. Rev. 86, 297–308.
Harlov, D.E., 2015. Apatite: a fingerprint for metasomatic processes. Elements 11 (3), 171–176.
Holser, W.T., 1997. Evaluation of the application of rare-earth elements to paleoceanography. Palaeogeogr. Palaeocl 132 (1-4), 309–323.
Hughes, J.M., Cameron, M., Mariano, A.N., 1991. Rare-earth-element ordering and structural variations in natural rare-earth-bearing apatites. Am. Mineral. 76 (7–8), 1165–1173.
Hughes, J.M., Rakovan, J.F., 2015. Structurally robust, chemically diverse: apatite and apatite supergroup minerals. Elements 11 (3), 165–170.
Ilyin, A.V., 1998. Rare-earth geochemistry of 'old' phosphorites and probability of syngenetic precipitation and accumulation of phosphate 1 In memory of Richard P. Sheldon 1. Chem. Geol. 144 (3-4), 243–256.
Jarvis, I., Burnett, W.C., Nathan, Y., Almbaydin, F.S.M., Attia, A.K.M., Castro, L.N., Flicoteaux, R., Hilmy, M.E., Husain, V., Qutawnah, A.A., Serjani, A., Zanin, Y.N., 1994. Phosphorite geochemistry - state-of-the-art and environmental concerns. Eclogae Geol. Helv. 87 (3), 643–700.
Kato, Y., Fujinaga, K., Nakamura, K., Takaya, Y., Kitamura, K., Ohta, J., Toda, R., Nakashima, T., Iwamori, H., 2011. Deep-sea mud in the Pacific Ocean as a potential resource for rare-earth elements. Nat. Geosci. 4 (8), 535–539.
Kynicky, J., Smith, M.P., Xu, C., 2012. Diversity of rare earth deposits: the key example of China. Elements 8 (5), 361–367.
Lee, S., Shen, Z., Xu, H., 2016. Study on nanophase iron oxyhydroxides in freshwater ferromanganese nodules from Green Bay, Lake Michigan, with implications for the adsorption of As and heavy metals. Am. Mineral. 101 (9), 1986–1995.
Li, X., Zhou, M.-F., 2015. Multiple stages of hydrothermal REE remobilization recorded in fluorapatite in the Paleoproterozoic Yinachang Fe-Cu-(REE) deposit, Southwest China. Geochim. Cosmochim. Ac 166, 53–73.
Liao, J., Sun, X., Li, D., Sa, R., Lu, Y., Lin, Z., Xu, L.i., Zhan, R., Pan, Y., Xu, H., 2019. New insights into nanostructure and geochemistry of bioapatite in REE-rich deep-sea sediments: LA-ICP-MS, TEM, and Z-contrast imaging studies. Chem. Geol. 512, 58–68.
Liu, X.Q., Zhang, H., Tang, Y., Yunlong, L., 2019. Effect of hydrothermal process on phosphorite type REE deposit in Zhijin, Guizhou: evidence from fluid inclusions. Acta Mineral. Sinica 39 (04), 403–411 (in Chinese with English abstract).
Liu, Y., Hu, Z., Gao, S., Günther, D., Xu, J., Gao, C., Chen, H., 2008. In situ analysis of major and trace elements of anhydrous minerals by LA-ICP-MS without applying an internal standard. Chem. Geol. 257 (1-2), 34–43.
Long, K.R., Van Gosen, B.S., Foley, N.K., Cordier, D., 2010. The principal rare earth elements deposits of the United States—a summary of domestic deposits and a global perspective. Scientific Investigations Report 2010-5220. US Geological Survey, 96.
Lumiste, K., Mänd, K., Bailey, J., Paiste, P., Lang, L., Lepland, A., Kirsimäe, K., 2019. REE +Y uptake and diagenesis in Recent sedimentary apatites. Chem. Geol. 525, 268–281.
Mao, T., Yang, R., Gao, J., Mao, J., 2015. Study of sedimentary feature of cambrian phosphorite and ore-controlling feature of old karst surface of the Dengying Formation in Zhijin, Guizhou. Acta Geol. Sinica 89 (12), 2374–2388 (in Chinese with English abstract).
Marchig, V., Gundlach, H., Möller, P., Schley, F., 1982. Some geochemical indicators for discrimination between diagenetic and hydrothermal metalliferous sediments. Mar. Geol. 50 (3), 241–256.
Meng, Q., Lan, A., Ye, C., Li, W., Wang, S., 2015. Investigation Report of Phosphorite (Rich in Rare Earth Elements) in Zhijin Area, Guizhou Province, Geology Brigade 104. Bureau of Geology and Mineral Exploration and Development, Guizhou Province (in Chinese).

Michard, A., Albarede, F., Michard, G., Minster, J.F., Charlou, J.L., 1983. Rare-earth elements and uranium in high-temperature solutions from east pacific rise hydrothermal vent field (13-degrees-N). Nature 303 (5920), 795–797.
Mitra, A., Elderfield, H., Greaves, M.J., 1994. Rare-earth elements in submarine hydrothermal fluids and plumes from the mid-Atlantic ridge. Mar. Chem. 46 (3), 217–235.
Orris, G.J., Grauch, R.I., 2002. Rare earth element mines, deposits and occurrences, 2. US Department of the Interior, US Geological Survey.
Peiravi, M., Dehghani, F., Ackah, L., Baharlouei, A., Godbold, J., Liu, J., Mohanty, M., Ghosh, T., 2021. A review of rare-earth elements extraction with emphasis on non-conventional sources: coal and coal byproducts, iron ore tailings, apatite, and phosphate byproducts. Min. Metall. Explor. 38 (1), 1–26.
Piper, D.Z., 1999. Trace elements and major-element oxides in the Phosphoria Formation at Enoch Valley, Idaho; Permian sources and current reactivities. 2331-1258, US Geological Survey.
Pu, X., Zhou, H., Wang, X., Luo, A., Li, S., Wang, J., Ye, H., Pan, X., Zeng, R., Huang, Z., Lin, M., 1993. Lithofacies Paleogeography and Mineralization of Cambrian in Southern China. Geological Publishing House, Beijing (in Chinese).
Rapp, J.F., Klemme, S., Butler, I.B., Harley, S.L., 2010. Extremely high solubility of rutile in chloride and fluoride-bearing metamorphic fluids: An experimental investigation. Geology 38 (4), 323–326.
Reynard, B., Lécuyer, C., Grandjean, P., 1999. Crystal-chemical controls on rare-earth element concentrations in fossil biogenic apatites and implications for paleoenvironmental reconstructions. Chem. Geol. 155 (3-4), 233–241.
Rona, P.A., 1978. Criteria for recognition of hydrothermal mineral-deposits in oceanic-crust. Econ. Geol. 73 (2), 135–160.
Ruttenberg, K.C., Berner, R.A., 1993. Authigenic apatite formation and burial in sediments from non-upwelling, continental-margin environments. Geochim. Cosmochim. Acta 57 (5), 991–1007.
Schenau, S.J., Slomp, C.P., De Lange, G.J., 2000. Phosphogenesis and active phosphorite formation in sediments from the Arabian Sea oxygen minimum zone. Mar. Geol. 169 (1-2), 1–20.
Service, R.F., 2010. Nations move to head off shortages of rare earths. Science 327 (5973), 1596–1597.
Shi, C., 2005. Formation of phosphorite deposit, Breakup of Rodinia supercontinent and Biology explosion - A case study of Weng' an, Kaiyang and Zhijin phosphorite deposits of Guizhou Province. Doctor of Philosophy Thesis, Institute of Geochemistry, Chinese Academy of Sciences, Guiyang, Guizhou, China (in Chinese with English abstract).
Slomp, C.P., Epping, E.H.G., Helder, W., Raaphorst, W.V., 1996. A key role for iron-bound phosphorus in authigenic apatite formation in North Atlantic continental platform sediments. J. Mar. Res. 54 (6), 1179–1205.
Suess, E., 1981. Phosphate regeneration from sediments of the Peru continental-margin by dissolution of fish debris. Geochim. Cosmochim. Acta 45 (4), 577–588.
Taylor, S.R., 1985. The continental crust: its composition and evolution. An examination of the geochemical record preserved in sedimentary rocks, 312.
Wang, Z., Ma, J., Li, J., Wei, G., Zeng, T., Li, L., Zhang, L., Deng, W., Xie, L., Liu, Z., 2018. Fe (hydro) oxide controls Mo isotope fractionation during the weathering of granite. Geochim. Cosmochim. Acta J. Geochem. Soc. Meteoritical Soc. 226, 1–17.
Wang, M., Sun, X., Ma, M., 2004. Rare Earth Elements Geochemistry and Genesis of Xinhua large-size phosphorite deposit in Western Guizhou. Min. Deposits 23 (04), 484–493 (in Chinese with English abstract).
Wei, S., Fu, Y., Liang, H., Ge, Z., Zhou, W., Wang, G., 2018. Re–Os geochronology of the Cambrian stage-2 and -3 boundary in Zhijin County, Guizhou Province, China. Acta 37 (2), 323–333.
Wright, J., Schrader, H., Holser, W.T., 1987. Paleoredox variations in ancient oceans recorded by rare-earth elements in fossil apatite. Geochim. Cosmochim. Acta 51 (3), 631–644.
Xing, C.-M., Wang, C.Y., 2017. Cathodoluminescence images and trace element compositions of fluorapatite from the Hongge layered intrusion in SW China: a record of prolonged crystallization and overprinted fluid metasomatism. Am. Mineral. 102 (7), 1390–1401.
Xu, C., Kynický, J., Smith, M.P., Kopriva, A., Brtnický, M., Urubek, T., Yang, Y., Zhao, Z., He, C., Song, W., 2017. Origin of heavy rare earth mineralization in South China. Nature Commun. 8 (1) https://doi.org/10.1038/ncomms14598.
Jiedong, Y., Weiguo, S., Zongzhe, W., Yaosong, X., Xiancong, T., 1999. Variations in Sr and C isotopes and Ce anomalies in successions from China: evidence for the oxygenation of Neoproterozoic seawater? Precambr. Res. 93 (2-3), 215–233.
Yang, R.D., Zhu, L.J., Wang, S.J., Jiang, L.J., Zhang, W.H., Gao, H., 2005. Negative Carbon Isotope Excursion in the Base Cambrian of Guizhou Province, China Implication for Biological and Stratigraphical Significance. Acta Geolofica Sinica (02), 157–164 (in Chinese with English abstract).
Yang, R.D., Wei, H.R., Bao, M., Wang, W., Wang, Q., Zhang, X.D., Liu, L., 2008. Discovery of hydrothermal venting community at the base of Cambrian barite in Guizhou Province, Western China: implication for the Cambrian biological explosion. Prog. Nat. Sci.
Yi, H., Peng, J., Xia, W., 1995. The Late Precambrian Paleo-Ocean Evolution of the Southeast Yangtze Continental Margin: REE Record. Acta Sedimentol. Sinica (04), 131–137 (in Chinese with English abstract).
Zhang, X., Zhai, S., Yu, Z., 2020. Strontium isotope compositions of hydrothermal barite from the Yonaguni IV: insight into fluid/sediment interaction and barite crystallization condition. J. Ocean Univ. China 19 (2), 377–385.
Zhou, K., Fu, Y., Ye, Y., Long, K., Zhou, W., 2019. Characteristics of the Rare Earth Elements' Accumulation of phosphorus rock series during the Early Cambrian, Guizhou Province. Acta Mineral. Sinica 39 (04), 420–431 (in Chinese with English abstract).
Zhu, R.X., Li, X.H., Hou, X.G., Pan, Y.X., Wang, F., Deng, C.L., He, H.Y., 2009. SIMS U-Pb zircon age of a tuff layer in the Meishucun section, Y unnan, southwest China: constraint on the age of the Precambrian-Cambrian boundary. Sci. China Ser. D-Earth Sci. 39 (08), 1105–1111 (in Chinese).